Improved Quantitation for PET/CT Image Reconstruction with System Modeling and Anatomical Priors

Adam M. Alessio, Paul E. Kinahan, and Thomas K. Lewellen

Imaging Research Laboratory, University of Washington Medical Center,
1959 NE Pacific St Box 356004, Seattle, WA USA 98195-6004

ABSTRACT

Accurate quantitation of PET tracer uptake levels in small tumors remains a challenge. This work uses an improved reconstruction algorithm to reduce the quantitative errors due to limited system resolution and due to necessary image noise reduction. We propose a method for finding and using the detection system response in the projection matrix of a statistical reconstruction algorithm. In addition we use aligned anatomical information, available in PET/CT scanners, to govern the penalty term applied during each image update. These improvements are combined with FORE rebinning in a clinically feasible algorithm for reconstructing fully 3D PET data. Simulated results show improved tumor bias and variance characteristics with the new algorithm.

Keywords: Anatomical Priors, PSF, segmentation, PET/CT, detector response, fully 3-D PET

1. INTRODUCTION

The quantitative accuracy of PET reconstructions is limited by several factors including the spatial resolution of the imaging system and the number of photons collected. System realities including, but not limited to, detector geometry, inter-crystal scatter, depth dependent sensitivity, crystal penetration, and detection electronics influence the overall resolution of a scanner resulting in variant resolution response and mispositioning errors. Moreover, PET imaging suffers from a limited number of photons resulting in noisy images that require some form of smoothing operation.

We propose using accurate system modeling and anatomical information in a clinically feasible reconstruction algorithm to reduce quantitative errors. The use of a system model, accounting for the detection system response, improves the spatial resolution of the reconstructions. Improved system models, with varying levels of complexity, have been successfully applied to high-resolution small animal PET systems.[1–6] The previous research described spatially variant system response in terms of coincident aperture functions,[7] system kernels,[1] detector response functions,[2] and detector blurring terms.[3,8] Our work employs a more general system response that models both the detection process and the effects of FORE rebinning. Therefore, our improved method uses a more general "system response function" (SRF).

PET/CT scanners offer the added advantage of aligned anatomical information that can be incorporated into the emission reconstruction algorithm to reduce image smoothness near the boundaries of tumors. This improvement allows for desirable noise properties in limited photon count scans while maintaining accurate tumor uptake levels. Several studies have explored the benefits of using anatomical information to guide reconstruction and noise regularization.[9–12]

2. SYSTEM RESPONSE FUNCTION

In a complete model, a whole-body PET system can be described by a 7 dimensional function with 4 dimension to describe the line interal domain and 3 dimensions to describe the spatial coordinates of the imaging volume. One choice of variables appears in figure 1 to describe $\mathrm{SRF}(u, v, \phi, \theta; x, y, z)$ where (u, v) defines the point on one detector surface where the coincident bin with azimuthal and axial angle (ϕ, θ) intersects. And, (x, y, z) defines the location in the volume that contributes to this coincident bin.

aalessio@u.washington.edu; phone 206 598-4521; depts.washington.edu/nucmed/IRL/

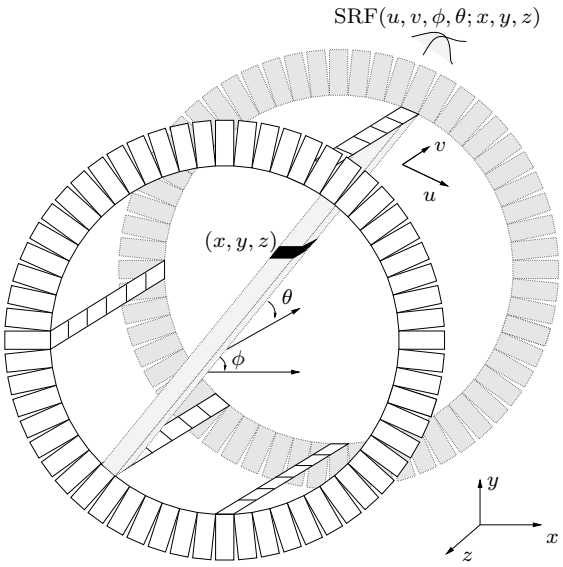

Figure 1. Illustration of fully characterized system response function, SRF, where (u, v) defines the point on one detector surface where the coincident bin with azimuthal and axial angle (ϕ, θ) intersects. And, (x, y, z) defines the location in the volume that contributes to this coincident bin.

Even though iterative reconstructions can accomodate more sophisticated and accurate models, all current PET systems use sub-optimal spatially invariant system models during reconstruction. In other words, they use a one dimensional system response function. Past efforts to model a spatially variant system blurring factor often use the 2 dimensional function, $\text{SRF}_{\text{2Dsimple}}(s; s_v)$, which blurs along radial bins in the sinograms (s, the distance between the z axis and the projection of the line onto a transaxial plane) and is spatially variant in radial distance s_v) (figure 2). The subscript v denotes the variables that parameterize the originating volume location as opposed to the line integrals. We will term this 2D funtion as a 1+1 because is blurs in one dimension and is variant in one dimension. This research employs a more complicated 2+1 SRF, which blurs in 2 dimensions and is variant in one dimension.

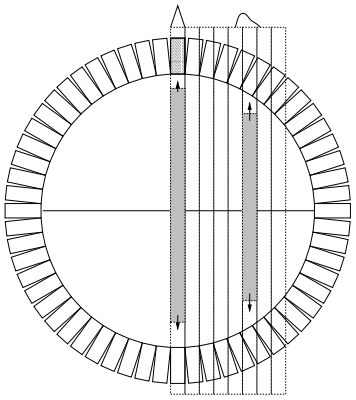

Figure 2. Depiction of the need for a 1+1 SRF. Photons from sinogram bins at edge of FOV can contribute to multiple detectors and be binned into erroneous sinogram bins. This $\text{SRF}_{2D_{simple}}(s_r; s)$ blurs data in radial position and is variant in radial position. Previous studies have used this form of SRF to account for non-uniform sinogram spacing, crystal pentration, and intercrystal scatter in high-resolution systems.

We employed Monte Carlo techniques to model the detection system of a fully 3D PET scanner.[13] Then, we performed FORE rebinning of the fully 3D data to reduce the data size leading to a clinically feasible

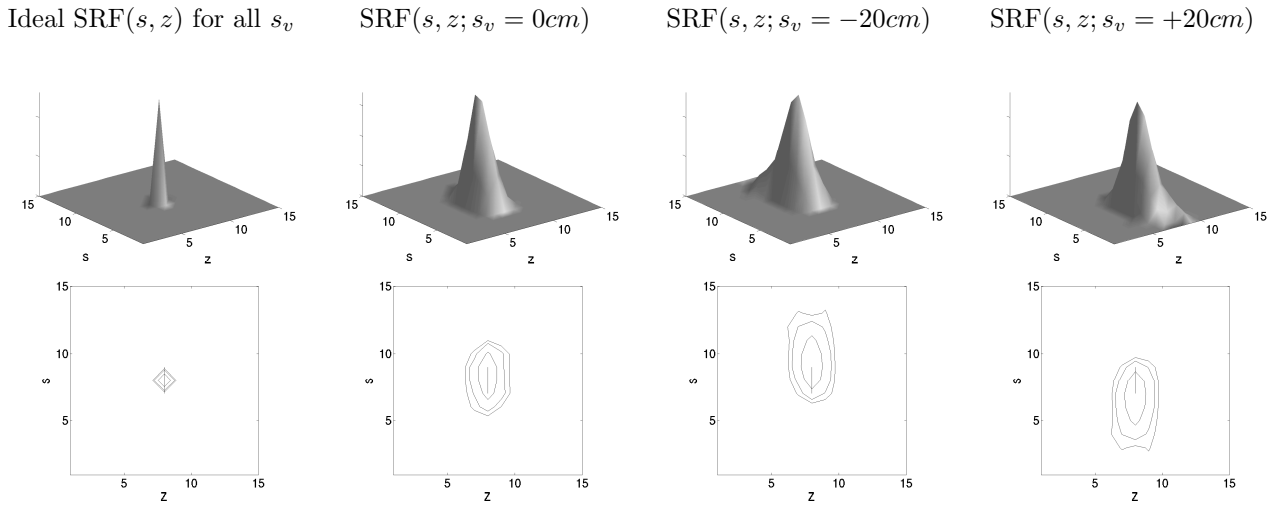

Figure 3. SRF$_(s,z;s_v)$ at different radial locations s_v for a transaxial FOV [-27.5cm, 27.5cm]. The second row presents the SRF as contour plots showing half, 5th, and tenth maximum contours, and marking the center of SRF from an ideal system with a cross.

reconstruction algorithm.[14] The 7 dimensional function describing this process was simplified to a 3 dimensional SRF. Specifically, we found the 2+1 SRF$(s,z;s_v)$ which blurs the ideal system matrix along radial bins (s) and axial planes (z) and is variant along radial bins (s_v). These dimensions were chosen from visual inspection of the resolution degradation in the data domain formed from point sources placed throughout the imaging volume. The radial bins followed by the axial bins received the greatest degradation and was most influenced by the radial positioning of the source. Figure 3 displays the SRF at varying radial positions.

The following summary outlines the steps performed to approximate the 3 dimensional SRF$(s,z;s_v)$. Using SimSET modified to account for discrete crystal elements, we simultated a whole body PET scanner with geometry and detectors similar to the GE Advance. Four fully 3D data sets were simulated from a point source at 4 different radial positions and FORE rebinned into sets of direct and cross planes. For a fixed ϕ, the (s,z) view of this data is the projection view of the data, as opposed to a sinogram view, and provides the desired system response information. The 4 data sets lead to measured response functions (s,z) at 4 radial positions s_v. The response functions at the remaining s_v are approximated by parameterizing the simulated (s,z) functions with discrete cosine transform coefficients. Then, a least-squares fit to a linear relationship amongst the coefficients from the 4 simulated response functions leads to coefficient values at all s_v and consequently, the complete SRF$(s,z;s_v)$.

3. ANATOMICAL BOUNDARY INFORMATION

PET/CT systems offer the added advantage for PET reconstruction of an aligned anatomical map. The anatomical map from the CT could be used in a variety of ways to govern image smoothness with the desire of reducing partial volume effects and improving quantitative accurary. Our past work explored using anatomical information post-reconstruction to improve upon conventional OSEM post-processing.[15] This work uses the CT data during the reconstruction.

The segmentation of aligned CT images supplies approximate boundary information of emission uptake regions, providing *a priori* image smoothness information. Specifically, in the simulation examples presented here, the edge detection was performed to find the boundary regions of known tumor locations. These regions were grown to approximately match the system resolution. Then, the regions were blurred with a 3D Gaussian to reduce errors from slight spatial mismatch.[16] Finally, these blurred regions defined the strength of a quadratic penalty term used in a penalized weighted least squares (PWLS) method.[17]

4. METHODS

4.1. Application

The improved SRF and boundary information were incorporated into the PWLS similarity measure

$$\Phi_{\mathrm{PWLS}}(x) = \frac{1}{2}(y - \mathbf{P}x)'\mathbf{W}(y - \mathbf{P}x) + \beta(x)G(x) \tag{1}$$

where the system matrix $\mathbf{P}$ times the estimate of the image x provides the current estimate of the conditional mean of the data, y. The weighting matrix, $\mathbf{W}$, is the inverse of an estimate of the conditional variances of the data.[17] The regularization term, $G(x)$, used for this study was a quadratic penalty

$$G(x_i) = \sum_{k \in N_{3D_i}} \frac{(x_i - x_k)^2}{d_{ik}} \tag{2}$$

where d_{ik} is the Euclidean distance between voxels i and k. The strength of the regularization term, β, was varied based on the boundary information. That is, β is less in boundary regions to preserve edges and is greater in constant activity regions. Finally, the objective function was optimized with iterative coordinate decent.[18]

The improved SRF's were incorporated into the system matrix $\mathbf{P}$. Since system memory was not a concern in this study, the system matrix was precomputed and blurred with the corresponding SRF. When $\mathrm{SRF}(s, z; s_v)$ was used, the method is termed "PWLS w/ 2+1". For comparison, the slightly more simple $\mathrm{SRF}(s; s_v)$ was also used and is termed "PWLS w/ 1+1".

4.2. Studies with Noiseless 2D Phantom

The proposed methods were first tested with a simple simulated phantom containing a constant background and 2 hot spots. Noiseless 2D data was generated from the phantom and modified to account for a realistic whole-body scanner system model.

4.3. Studies with Whole-body phantom

The methods were also tested with simulated fully 3D measurements from a whole-body phantom. The phantom represents a typical body size and contained 24 spherical lesions of varying sizes and contrast levels in varying background levels. These measurements included noise properties similar to a real system, essentially incorporating the influence of true, random, and scattered coicidences.[19] The effect of attenuation was also included in the simulations. After correcting the data in the fully 3D domain, the measurements were FORE rebinned in preparations for 2D image reconstruction. We simulated 50 noise realzations of the fully 3D measurements.

5. RESULTS

5.1. Noiseless 2D Phantom

Figure 4 presents reconstructions from the simple 2D phantom. Profiles through the reconstruction highlight the resolution and quantitative accuracy of the methods. The PWLS methods used the same global regularization strength. The PWLS w/ boundary information in the prior significantly improves the edges of the tumors. The SRF improved the accuracy of the background and tumor levels. Clearly, the combination of the SRF and boundary information yielded the best results in edge preservation and tumor levels.

5.2. Whole-body phantom

Figure 5 displays reconstructions using the different methods tested with the whole-body phantom. Images were chosen with similar noise properties. FBP used an 80% cutoff Hanning window, the OSEM reconstruction was post-smoothed with a 10mm 3D Gaussian filter, and all of the PWLS reconstructions used the same global prior term and were iterated to convergence. The use of the system matrix in the reconstruction slightly reduced the convergence rate of PWLS as shown in figure 6, but not enough to effect overall reconstruction time.

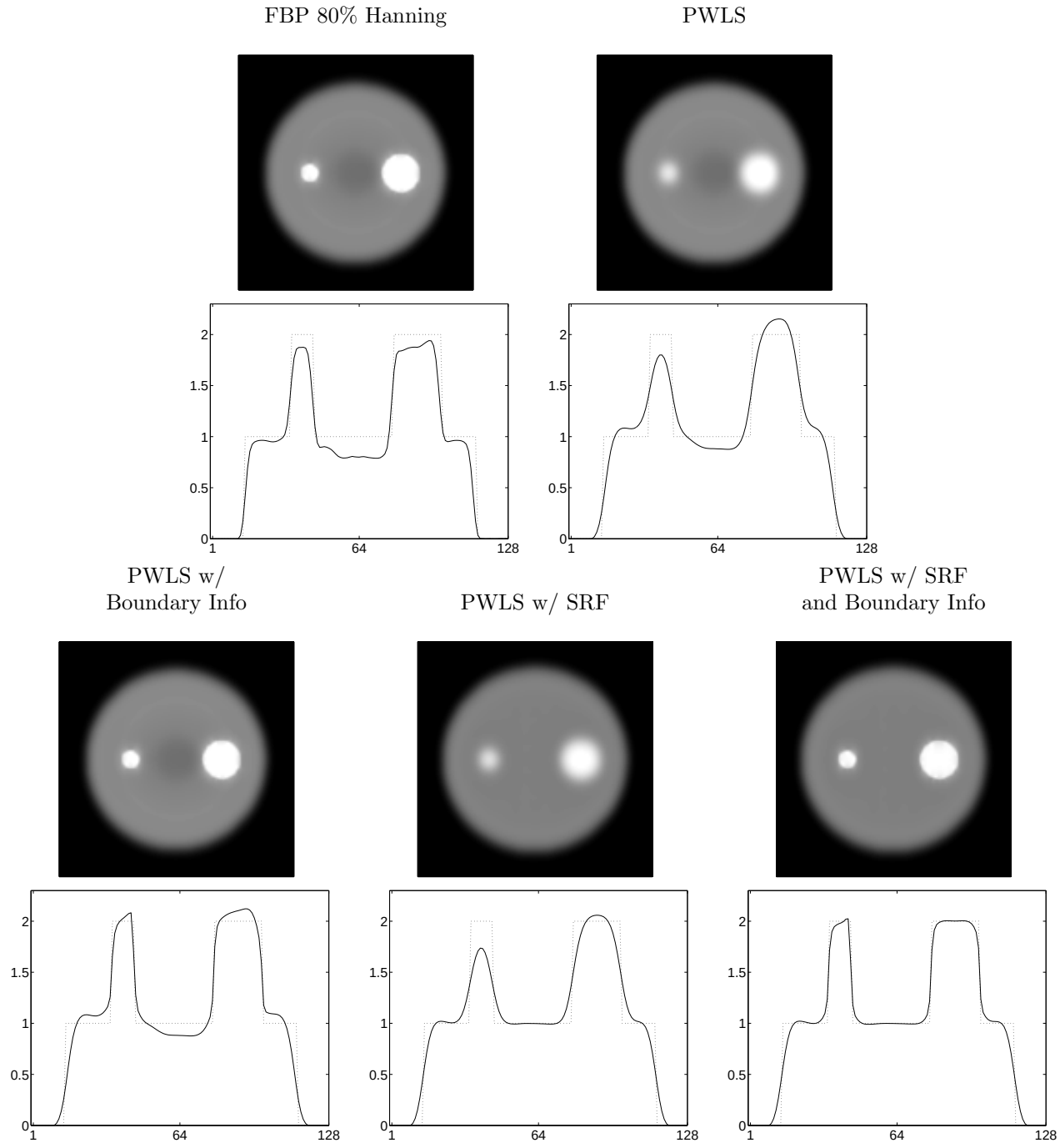

Figure 4. Noiseless 2D sample case showing benefit of system response function and boundary prior information in the reconstruction. Each reconstruction is displayed with a horizontal profile through the reconstruction (solid line) and through the true object (dotted line). The benefit is more pronounced with the smaller object.

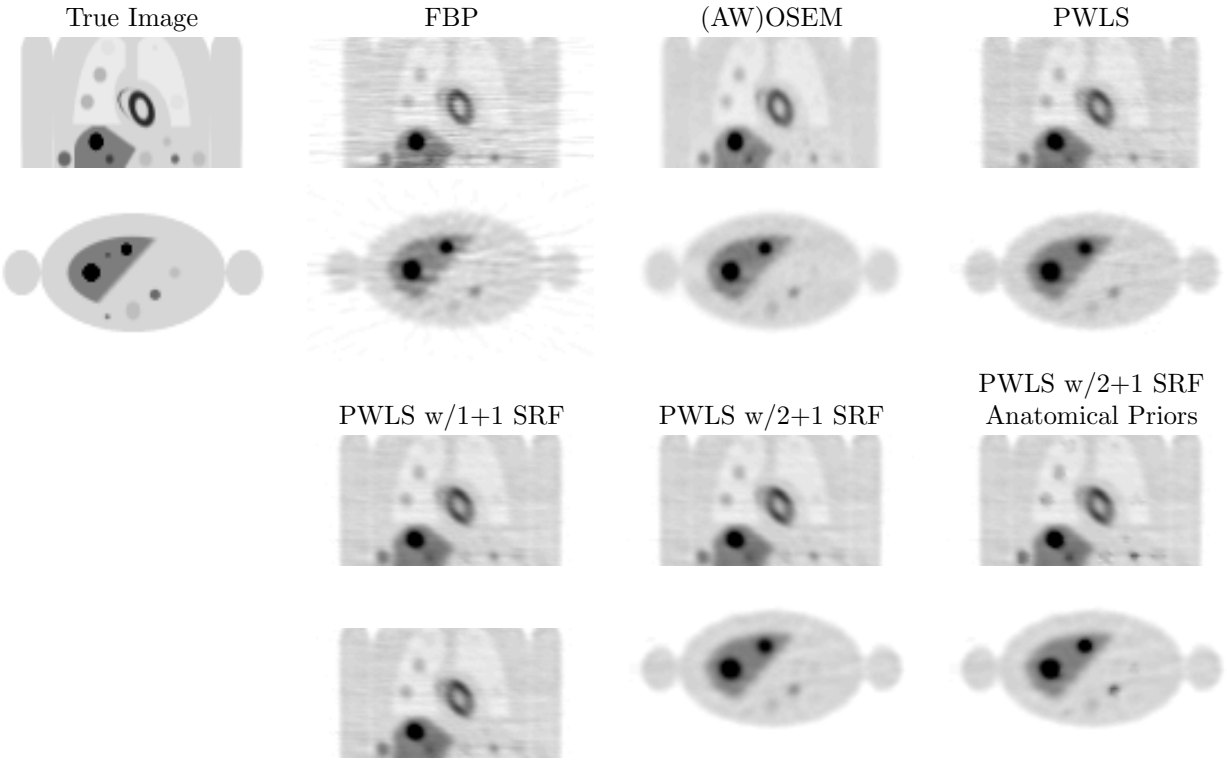

Figure 5. Coronal and transaxial slices through reconstructions of a single noise realization of the simulated whole-body phantom.

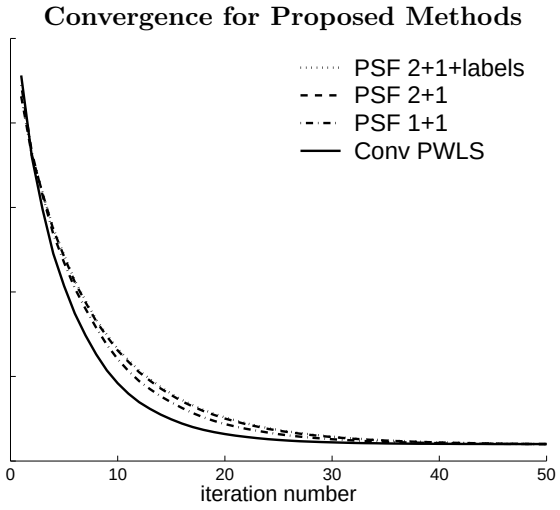

Figure 6. $\Phi(x)$ vs. iteration number of the PWLS algorithms used with whole-body PET measurements. Convergence is slightly slower when the system response function is included.

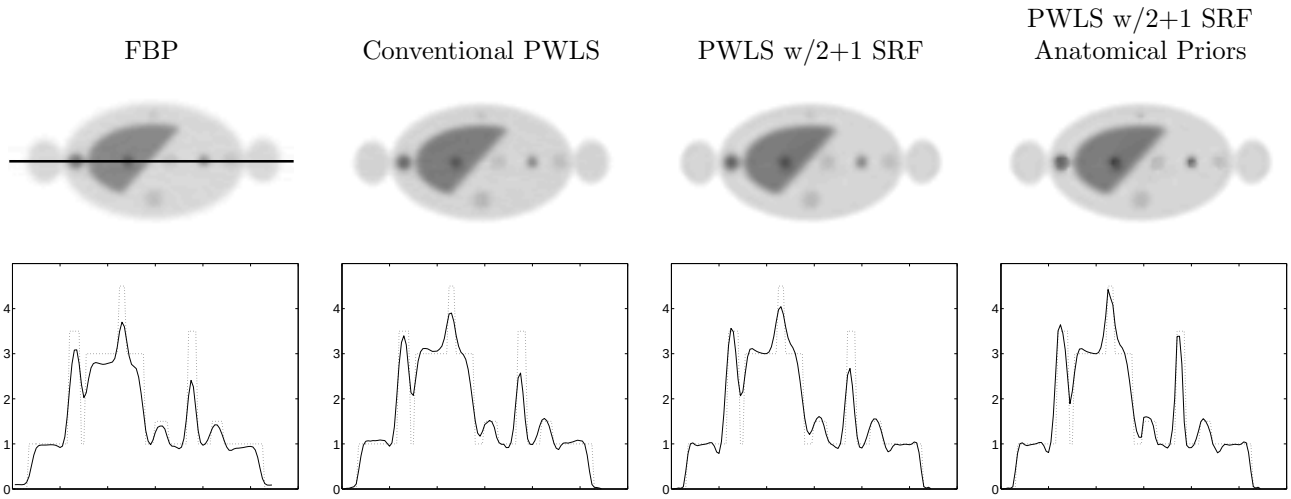

Figure 7. Transaxial slice through mean images of 50 noise realizations. The second row plots the horizontal profile through the slice with a solid line and the profile through the true object with a dotted line.

Figure 7 displays the mean images from 50 reconstructions of the 50 different noise realizations. The smoothing parameter for each method was set to have similar noise properties in the images. The second row of the figure plots profiles through 5 tumors in the images along with the profile of the true object. The use of the SRF slightly improves the quantitation over conventional PWLS and the use of the SRF and labels greatly improves the quantitation in this single slice.

Figure 8 plots the bias in max tumor values versus the variance in the max values. Each datum point was computed from 50 whole-body reconstructions and represents the average over 8 tumors (2cm and 3cm tumors). The curves are presented on two plots to avoid confusion. In this analysis, the PWLS w/2+1 method provides improved accuracy at a majority of noise levels.

Similarly, figure 9 plots the bias in the mean of each tumor volume of interest. This figure of merit provides insight into the accuracy of the whole tumor volume (not just max value of tumor). Once again, the PWLS w/2+1 offers the best performance at most noise levels.

6. CONCLUSIONS

An improved system model and aligned anatomical information was successfully incorporated into a reconstruction algorithm and tested with simulated data. Individual reconstructions highlighted strong quantitative benefits of using the improved SRF and using the boundary information supplied in the anatomical images. The initial quantitative analysis across multiple realizations and at a variety of image smoothing levels reveals only modest improvements with the new methods. This analysis needs to be exanded to include more tumor sizes and figures of merit before a final conclusion can be drawn regarding the efficacy of the proposed methods.

These methods could be utilized on modern PET/CT scanners although several open problems need to be solved. Namely, the current system model is done solely through simulations and a scheme needs to be developed for empirical modeling on modern systems. Secondly, the use of CT scans for anatomical information raises the challenge of accurately segmenting CT images into regions of expected emission tracer uptake. The positive results presented here justify our efforts to find solutions to these challenges.

ACKNOWLEDGMENTS

This work was supported by NIH grants CA74135 and CA42593.

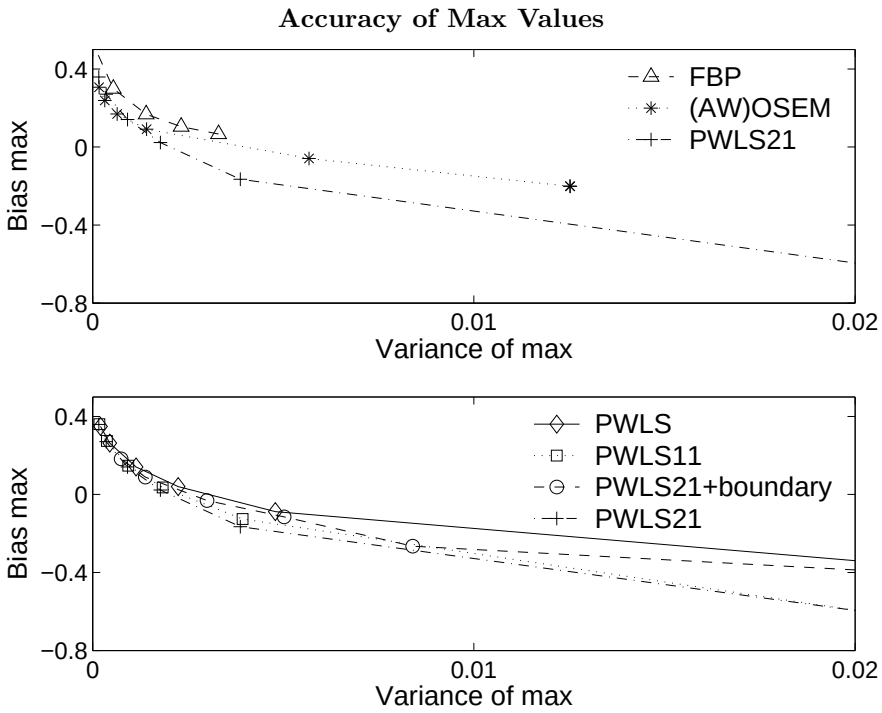

Figure 8. Mean bias of max tumor values versus variance of max values across 50 realizations averaged over 8 tumors. The curves are formed from varying the smoothing parameter for each method (cut-off of Hanning window for FBP, FWHM of post-smoothing Gaussian used for OSEM, and β for PWLS methods).

REFERENCES

1. T. Frese, N. C. Rouze, C. A. Bouman, K. Sauer, and G. D. Hutchins, "Quantitative comparison of FBP, EM, and Bayesian reconstruction algorithms for the IndyPET scanner," *IEEE Trans Med Imaging* **22**(2), pp. 258–76, 2003.
2. V. V. Selivanov, Y. Picard, J. Cadorette, S. Rodrigue, and R. Lecomte, "Detector response models for statistical iterative image reconstruction in high resolution PET," *IEEE Trans Nuclear Science* **47**(3), pp. 1168–1175, June 2000.
3. E. U. Mumcuoglu, R. M. Leahy, S. R. Cherry, and E. Hoffman, "Accurate geometric and physical response modelling for statistical image reconstruction in high resolution PET," in *Proc. of IEEE Nucl. Sci. Symp. and Med. Imaging Conf.*, **3**, pp. 1569–1573, 1996.
4. G. Boning, B. J. Pichler, M. Rafecas, E. Lorenz, M. Schwaiger, and S. I. Ziegler, "Implementation of Monte Carlo coincident aperture functions in image generation of a high-resolution animal positron tomograph," *IEEE Trans Nuclear Science* **48**(3), pp. 805–810, 2001.
5. Z. Liang, "Detector response restoration in image reconstruction of high resolution positron emission tomography," *IEEE Trans Med Imaging* **13**(2), pp. 314–321, June 1994.
6. D. Strul, R. B. Slates, M. Dahlbom, S. R. Cherry, and P. K. Marsden, "An improved analytical detector response function model for multilayer small-diameter PET scanners," *Phys Med Biol* **48**(8), pp. 979–994, 2003.
7. D. Schmitt, B. Karuta, C. Carrier, and R. Lecomte, "Fast point spread function computation from aperture functions in high-resolution positron emission tomography," *IEEE Trans Med Imaging* **7**(1), pp. 2–12, 1988.
8. K. Lee, P. E. Kinahan, J. A. Fessler, R. S. Miyaoka, M. Janes, and T. K. Lewellen, "Pragmatic fully 3D image reconstruction for the MiCES mouse imaging PET scanner," *Physics in Medicine and Biology* **49**(19), p. 4563, 2004.

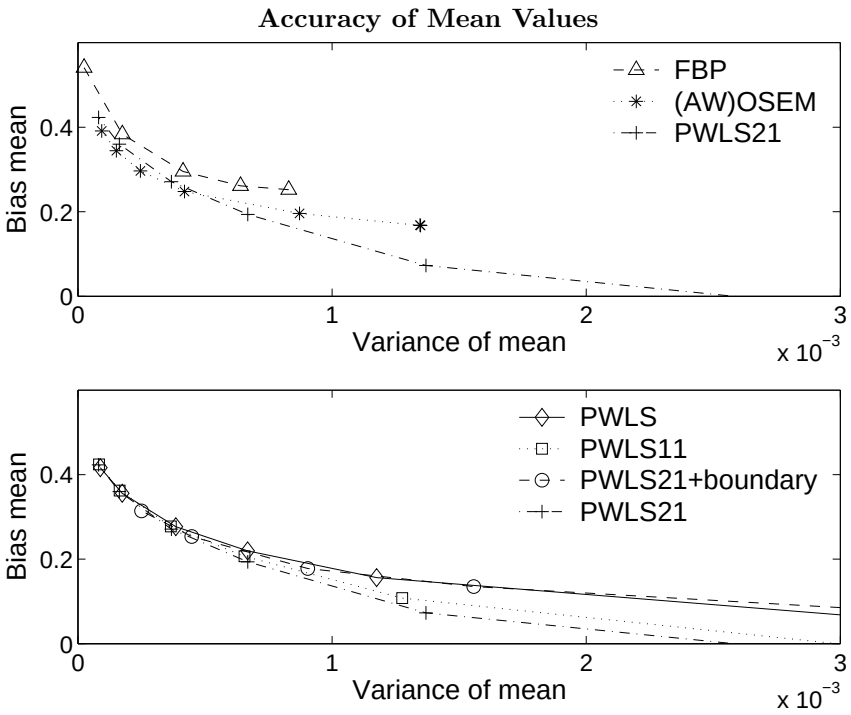

Figure 9. Mean bias of mean tumor values versus variance of mean values across 50 realizations averaged over 8 tumors. The curves are formed from varying the smoothing parameter for each method.

9. J. A. Fessler, N. H. Clinthorne, and W. L. Rogers, "Regularized emission image reconstruction using imperfect side information," *IEEE Trans Nuclear Science* **39**(5), pp. 1464–71, 1992.
10. G. Gindi, M. Lee, A. Rangarajan, and I. G. Zubal, "Bayesian reconstruction of functional images using anatomical information as priors," *IEEE Trans Med Imaging* **12**(4), pp. 670–680, 1993.
11. X. Ouyang, W. H. Wong, V. E. Johnson, X. Hu, and C. Chen, "Incorporation of correlated structural images in PET image reconstruction," *IEEE Trans Med Imaging* **13**(4), pp. 627–640, 1994.
12. J. E. Bowsher, V. E. Johnson, and e. al., "Bayesian reconstruction and use of anatomical a priori information for emission tomography," *IEEE Trans Med Imaging* **15**(5), pp. 673–86, 1996.
13. T. K. Lewellen, R. L. Harrison, and S. Vannoy, "The SimSET program in Monte Carlo calculations," in *Monte Carlo Calculations in Nuclear Medicine*, M. Ljungberg, S. Strand, and M. King, eds., pp. 77–92, IOP Publishing, Philadelphia, PA, 1998.
14. M. Defrise, P. E. Kinahan, D. W. Townsend, C. Michel, M. Sibomana, and D. F. Newport, "Exact and approximate rebinning algorithms for 3D PET data," *IEEE Trans Med Imaging* **16**(2), pp. 145–158, 1997.
15. P. M. Cheng, P. Kinahan, A. Alessio, H. J. Vesselle, S. Pathak, L. Ng, C. Comtat, M. Defrise, and T. Lewellen, "Post-reconstruction partial volume correction in PET/CT imaging using CT information," in *Radiological Society of North America*, (Chicago), 2004.
16. C. Comtat, P. E. Kinahan, J. A. Fessler, T. Beyer, D. W. Townsend, M. Defrise, and C. Michel, "Clinically feasible reconstruction of 3D whole-body PET/CT data using blurred anatomical labels," *Phys Med Biol* **47**, pp. 1–20, 2002.
17. J. A. Fessler, "Penalized weighted least-squares image reconstruction for positron emission tomography," *IEEE Trans Med Imaging* **13**(2), pp. 290–299, 1994.
18. C. A. Bouman and K. Sauer, "A unified approach to statistical tomography using coordinate descent optimization," *IEEE Trans. on Image Processing* **5**(3), pp. 480–492, 1996.
19. C. Comtat, P. E. Kinahan, M. Defrise, C. Michel, C. Lartizien, and D. W. Townsend, "Simulating whole-body PET scanning with rapid analytical methods," *IEEE Nuclear Science Symposium* **3**, pp. 1260–1264, 1999.